


Article

Role of Potassium Substitution in the Magnetic Properties and Magnetocaloric Effect in $\text{La}_{0.8-x}\text{K}_x\text{Ba}_{0.05}\text{Sr}_{0.15}\text{MnO}_3$ ($0 \leq x \leq 0.20$)

Dhawud Sabilur Razaq¹, Budhy Kurniawan^{1,*}, Dicky Rezky Munazat¹, Kazumitsu Watanabe² and Hidekazu Tanaka²

¹ Department of Physics, Universitas Indonesia, Depok 16424, Indonesia; dhawud.sabilur@sci.ui.ac.id (D.S.R.); dicky.rezky@sci.ui.ac.id (D.R.M.)

² Department of Physics, Tokyo Institute of Technology, Meguro-Ku, Tokyo 152-8551, Japan; watanabe.k@ee.phys.titech.ac.jp (K.W.); tanaka@ee.phys.titech.ac.jp (H.T.)

* Correspondence: budhy.kurniawan@sci.ui.ac.id; Tel.: +62-821-2320-0619

Received: 19 April 2020; Accepted: 16 May 2020; Published: 19 May 2020



Abstract: The magnetic and magnetocaloric effects of potassium-substituted $\text{La}_{0.8-x}\text{K}_x\text{Ba}_{0.05}\text{Sr}_{0.15}\text{MnO}_3$ ($0 \leq x \leq 0.20$) manganite were explored. The samples in polycrystalline form were synthesized by the sol–gel method, with a final sintering temperature of 1100 °C. Powder X-ray diffraction (XRD) patterns refined by Rietveld refinement show that all samples crystallized in rhombohedral structure with R-3c space group. The unit cell volume of the samples decreases with increasing potassium concentration. In addition, small changes in average bond length and bond angle are also observed in the samples. Scanning electron microscope (SEM) images reveal that the largest average grain size was observed for $x = 0.10$. Field-cooled (FC) magnetization measurements show that the Curie temperature (T_C) of the samples increases from 320 K for $x = 0$ to 360 K for $x = 0.2$. The largest magnetocaloric (MCE) effect, which is represented by maximum magnetic entropy change ($-\Delta S_{M, MAX}$), reaches its greatest value for the $x = 0.10$ sample. The monotonous increase in T_C suggests that T_C is mainly governed by the ferromagnetic coupling between Mn ions induced by the changes on average bond length and bond angle. The obtained $-\Delta S_{M, MAX}$ value suggests that MCE property is more sensitive to Zener theory of double exchange, which is strongly related to the $\text{Mn}^{3+}/\text{Mn}^{4+}$ ratio of the samples.

Keywords: double exchange; magnetic; magnetocaloric; perovskite manganite

1. Introduction

The demand for alternative refrigerant technology has significantly increased in the last decade. This is due to the use of harmful substances in conventional vapor compression technology, which is also involved in the ozone depletion phenomenon. To overcome this issue, magnetic refrigerant technology has been proposed and developed. Magnetic refrigerant technology uses the principle of the magnetocaloric effect (MCE) property of ferromagnetic materials [1]. MCE can be defined as the ability of ferromagnetic materials to change its temperature in the presence of an external magnetic field [1]. This makes MCE an environmentally friendly technology and, thus, can contribute to limit the use of harmful substances in the refrigerant system. MCE property of ferromagnetic materials can be represented by two expressions which are magnetic entropy change (ΔS_M) and adiabatic temperature change (ΔT_{ad}) [2]. These two expressions arise from two different methods, which were used to observe the magnitude of the MCE property [3]. Of these two expressions, ΔS_M is usually the most used expression in research on the MCE property, due to the simplicity of the experimental set up.

The main objective in researching the MCE property of ferromagnetic materials is finding a material that has a large ΔS_M value. Additionally, this large ΔS_M value needs to occur at near room

temperature with a sufficiently large Relative Cooling Power (RCP) value. RCP value can be defined as the efficiency of the MCE property. Large RCP values indicate the working temperature range of the magnetocaloric material without losing more than 50% of its maximum ΔS_M value. In the beginning, pure Gd metals and Gd-based alloys were found to exhibit large ΔS_M values near room temperature [4,5]. However, the expensive cost of Gd (4000 \$/kg) sets a limitation on the development of magnetic refrigerant technology. To overcome this limitation, exploration to find another possible candidate for magnetocaloric materials, such as MnAs-based alloys, LaFeSi alloys, and LaMnO₃ (LMO)-based compounds, has been conducted [6–8]. Among these groups, LMO-based compounds have been demonstrated to possess unique properties that are not found in the other mentioned candidates, including colossal magnetoresistance (CMR), microwave absorbance, and solid oxide fuel cells (SOFC) [9–11]. Additionally, its high chemical stability and simple sample preparation method have led to an increase in the interest in further studying the MCE property of this material [12–15].

Currently, optimization in ΔS_M value is the main objective in research regarding the MCE property of LMO-based compounds. In LMO-based compounds, there are several factors that can be regarded as the reason behind the increase in the $-\Delta S_M$ value. These factors are the Mn³⁺/Mn⁴⁺ ratio, average A-site ionic radius ($\langle r_A \rangle$), and A-site cationic mismatch (σ^2). According to previous research, the $-\Delta S_M$ value of LMO-based compounds is expected to increase until the value of Mn³⁺/Mn⁴⁺ ratio reaches around 7/3 or 2/1 [16,17]. Beyond this ratio, the $-\Delta S_M$ value is expected to decrease monotonously as Mn⁴⁺ content increases. Examples of this can be found in La_{1-x}Ca_xMnO₃ and La_{1-x}Sr_xMnO₃ [18,19]. On the other hand, there are several cases where $-\Delta S_M$ value increases with the increase in $\langle r_A \rangle$ and σ^2 . Examples of this can be seen in La_{0.6}Ca_{0.4-x}Sr_xMnO₃, La_{0.7-x}Dy_xCa_{0.3}MnO₃, and La_{0.5}Ca_{0.5-x}Pb_xMnO₃ [20–22]. However, special consideration is needed when dealing with a more complex LMO-based compounds, especially potassium (K⁺)-substituted LMO-based compounds. This is due to the fact that monovalent ion converts twice the amount of Mn³⁺ to Mn⁴⁺ ion and the fact that K⁺ ion has the largest ionic radius among monovalent ions, which is commonly substituted to LMO-based compounds [23–26]. There have been some cases where substitution of K⁺ ion increased the maximum $-\Delta S_M$ value of LMO-based compounds. Examples of this can be seen in La_{0.7}Sr_{0.2}M_{0.1}MnO₃ (M = Na, K), La_{0.7}M_{0.2}M'_{0.1}MnO₃ (M = Sr, Ba and M' = Na, Ag, K), and La_{0.75}Ba_{0.1}M_{0.15}MnO₃ (M = Na, Ag, and K) [27–29]. On the other hand, there have been several cases where substitution of K⁺ ion reduced the maximum $-\Delta S_M$ value of LMO-based compounds. Examples of this can be seen in La_{0.8}Ag_{0.2-x}K_xMnO₃ and La_{0.65}M_{0.3}M'_{0.05}MnO₃ (M = Ba, Ca and M' = Ba, Ag, K) [30,31]. The mentioned results show that the main factor behind the evolution of $-\Delta S_M$ value in K⁺ ion substituted LMO-based compounds is still open to debate.

To investigate the most dominant factor behind the changes in the $-\Delta S_M$ value of a K⁺ ion substituted LMO-based compounds, a comprehensive study on the MCE property of La_{0.8-x}K_xBa_{0.05}Sr_{0.15}MnO₃ ($0 \leq x \leq 0.20$) was performed. La_{0.8}Ba_{0.05}Sr_{0.15}MnO₃ was chosen to be the parent compound, because the combination of Ba and Sr ions in La-Ba-Sr-MnO₃ compound is less studied than other substituted LMO-based compounds such as La-Ba-Ca-MnO₃ and La-Ca-Sr-MnO₃ [4,8,32]. Additionally, the combination of Ba and Sr ions in the A-site of perovskite structure has the potential to exhibit a large $-\Delta S_M$ value in perovskite manganite compounds. This is proved by the results obtained by Phan et al. in La_{0.6}Ba_{0.2}Sr_{0.2}MnO₃ ($-\Delta S_M = 2.26$ J/kg K at 1 T), Banik et al. in Pr_{0.7}Ba_{0.16}Sr_{0.14}MnO₃ ($-\Delta S_M = 4.80$ J/kg K at 5 T), and Pham et al. in Pr_{0.7}Ba_{0.1}Sr_{0.2}MnO₃ ($-\Delta S_M = 5.67$ J/kg K at 5 T) [33–35]. Additionally, the composition of Ba ion was determined to be less than Sr ion with the expectation that the resulting compound will demonstrate a large $-\Delta S_M$ value as seen in Pr_{0.7}Ba_{0.1}Sr_{0.2}MnO₃. With a constant composition of divalent ions (Ba²⁺ and Sr²⁺), the substitution of La³⁺ ion by K⁺ ion in La_{0.8-x}K_xBa_{0.05}Sr_{0.15}MnO₃ will increase the population of Mn⁴⁺ ion while simultaneously decreasing the population of Mn³⁺ ion to preserve charge neutrality. This condition will affect the Mn³⁺/Mn⁴⁺ ratio of the samples. Additionally, the large ionic radius of K⁺ ion will ensure that $\langle r_A \rangle$ ($\langle r_A \rangle = \sum x_i r_i$; x_i is the fractional occupancy of A-site ions and r_i is the corresponding ionic radius) and σ^2 ($\sigma^2 = \langle r_A^2 \rangle - \langle r_A \rangle^2$; $\langle r_A^2 \rangle = \sum x_i r_i^2$) will only increase as

the concentration of K^+ ion increases. This experimental setup will help to investigate which of the mentioned factors (Mn^{3+}/Mn^{4+} ratio, $\langle r_A \rangle$, and σ^2) that is more dominant in affecting the evolution of $-\Delta S_M$ value in $La_{0.8-x}K_xBa_{0.05}Sr_{0.15}MnO_3$ ($0 \leq x \leq 0.20$).

2. Materials and Methods

Polycrystalline $La_{0.8-x}K_xBa_{0.05}Sr_{0.15}MnO_3$ ($0 \leq x \leq 0.20$) samples, denoted as LKBS-0 ($x = 0$), LKBS-05 ($x = 0.05$), LKBS-10 ($x = 0.10$), LKBS-15 ($x = 0.15$), and LKBS-20 ($x = 0.20$) in powder form were prepared using the sol-gel method. A stoichiometric amount of La_2O_3 , KNO_3 , $Ba(NO_3)_2$, $Sr(NO_3)_2$, $Mn(NO_3)_2 \cdot 4H_2O$, and $C_6H_8O_7 \cdot H_2O$ were initially dissolved in double-distilled water. In this experiment, La_2O_3 needs to be converted into nitrate form by reacting with nitric acid. Citric acid was used in the present work as a metal ion complexant and as a fuel during the combustion process. The amount of citric acid can be calculated from the ratio of citric acid (CA) to total metal nitrate (MN) equal to 1:1.2 [36,37]. All the dissolved precursors were mixed together into a single solution and then heated until the temperature of the solution reaches 80 °C. Afterward, the pH of the solution was adjusted until it reaches around 7 by adding ammonium solution, and then the solution was left to evaporate under constant stirring until a viscous gel is formed. The resulting gel was dehydrated until a dried gel was formed and then calcined at 550 °C to liberate the organic compound inside the gel. Pre-calcination was done at 900 °C to make sure there was no organic compound left in the sample. The powder samples were pressed into a pellet with axial pressure about 10 tons for approximately 10 min in order to obtain a square-shaped bulk with 12 mm sides. Sample preparation was completed with sintering process at 1100 °C for 12 h.

The crystal structure and phase purity of the samples were examined using powder X-ray Diffraction (XRD) using Cu- α radiation ($\lambda = 1.54059 \text{ \AA}$) at room temperature. The diffraction angle was recorded in an angular range from 10° to 90° with a step size of 0.02°. In the present work, the Rietveld refinement process was carried out using the General Structure and Analysis software II (GSAS-II) [38]. The morphology of the samples was examined with a scanning electron microscope (SEM). The chemical composition, as well as its distribution, was examined using Energy Dispersive X-ray (EDX) with the elemental mapping method. The magnetic properties of the sample were determined using magnetic properties measurement system (MPMS).

3. Results

3.1. Structural and Morphology Analysis

The powder diffraction patterns of $La_{0.8-x}K_xBa_{0.05}Sr_{0.15}MnO_3$ ($0 \leq x \leq 0.20$) samples measured at room temperature are shown in Figure 1. There is almost no significant difference in the powder diffraction pattern of samples that were substituted by K^+ ion. This implies that substituting up to 20% K^+ ion into the samples does not affect the crystal structure of the samples. This argument is also supported by the result of the Rietveld refinement process, which shows that the Miller indices of all the samples belong to the rhombohedral structure with R-3c space group. Furthermore, Rietveld refinement process also proves that all samples are single phase without any detectable impurities. The structural parameters obtained through the Rietveld refinement process are listed in Table 1.

Substitution with K^+ ion is observed to slightly reduce the unit cell volume. This can be correlated with the increasing concentration of Mn^{4+} ion, which has the smallest ionic radius within the samples, due to the substitution of La^{3+} by K^+ ion. Similar cases where the unit cell volume of LMO-based compounds decreased due to substitution by larger ion have been observed by Shaikh and Varshney in $La_{1-x}K_xMnO_3$ ($x = 0.1$; 0.125; and 0.15) compounds and Chebanee et al. in $La_{0.65}Ce_{0.05}Sr_{0.3}Mn_{1-x}Cu_xO_3$ ($0 \leq x \leq 0.15$) compounds [39,40]. Substitution by K^+ ion also increases the $\langle r_A \rangle$ from 1.243 to 1.310 for LKBS-0 and LKBS-20, respectively. This, in turn, causes the values of Goldschmidt tolerance factor, t_G , and σ^2 to have an increasing trend from 0.930 to 0.965 and 3.833×10^{-3} to 18.101×10^{-3} , respectively.

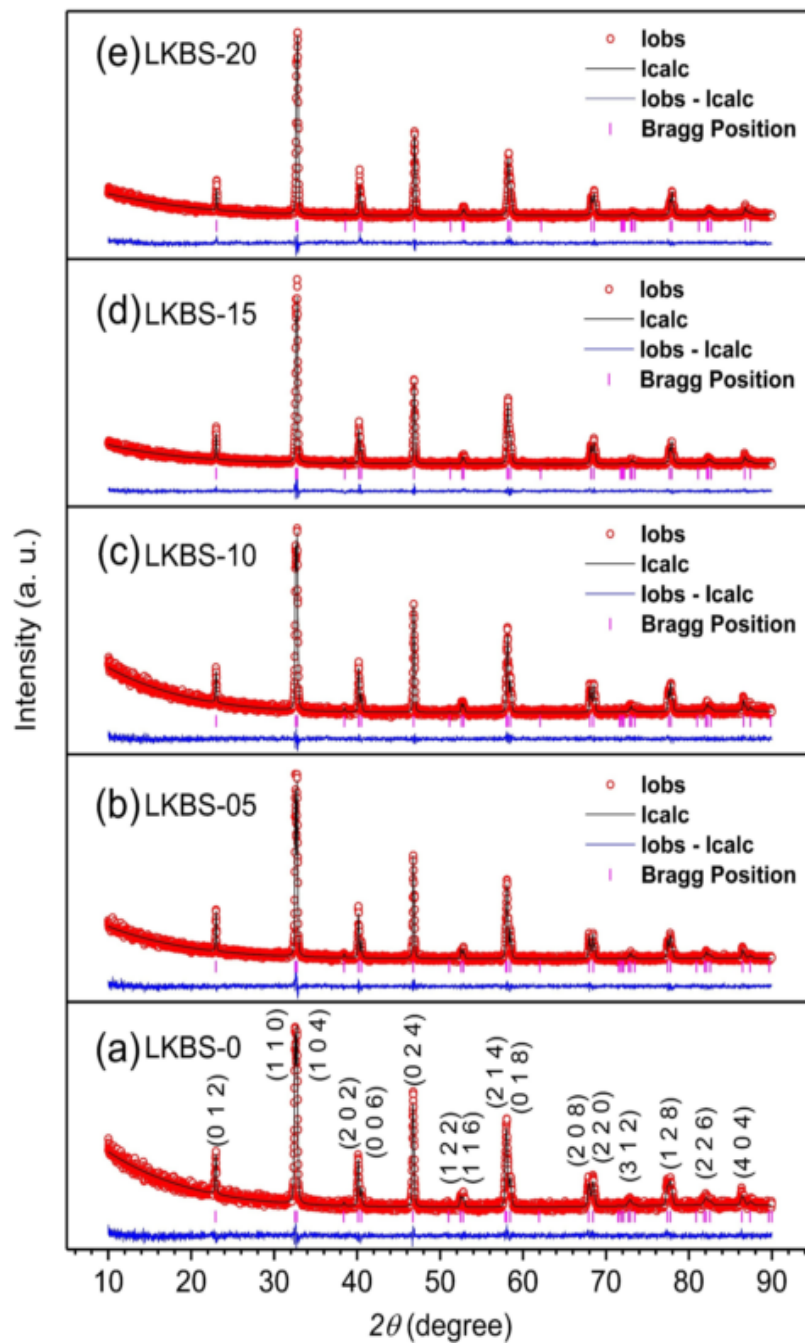


Figure 1. Powder diffraction pattern and the corresponding Rietveld refinement of $\text{La}_{0.8-x}\text{K}_x\text{Ba}_{0.05}\text{Sr}_{0.15}\text{MnO}_3$ ($0 \leq x \leq 0.20$) samples. (a) LKBS-0; (b) LKBS-05; (c) LKBS-10; (d) LKBS-15 and (e) LKBS-20.

The average crystallite size of all samples was calculated using two different methods, namely the Scherrer method and the Williamson-Hall method. The calculation of the average crystallite from the Scherrer method can be performed by following the equation given as [41]:

$$C_{SCH} = \frac{0.9 \lambda}{\beta \cos \theta} \quad (1)$$

where C_{SCH} is the average crystallite size from the Scherrer method, λ is the wavelength of Cu-K α radiation (1.5406 Å), θ is the corresponding diffraction peaks from powder diffraction patterns, and β is the full-width at half maximum (FWHM) of each corresponding diffraction peaks. In the present

work, only the prominent peaks were used to calculate the $\beta \cos \theta$ value. Alternatively, the calculation of average crystallite size can also be performed using the W-H plot. The average crystallite size can be obtained from the linear fit of the $4 \sin \theta$ versus $\beta \cos \theta$ graph according to the following equation [42]:

$$\beta \cos \theta = \frac{0.9 \lambda}{C_{W-H}} + 4\epsilon \sin \theta \quad (2)$$

where C_{W-H} is defined as the average crystallite size from W-H method, β is defined as $\beta = \sqrt{\beta_{exp}^2 - \beta_s^2}$. Here, β_{exp} is the FWHM estimated from powder diffraction pattern and β_s is the FWHM of a standard silicon sample. The intercept with the y-axis will show the value of average crystallite size (C_{W-H}), and the gradient of the slope will show the strain effect (ϵ) on the crystallites. The average crystallite size calculated using the Scherrer method and the W-H plot is listed in Table 1. The average crystallite size obtained from the W-H plot is larger compared to that obtained from the Scherrer method. This is due to the fact that the Scherrer method excludes the effect of strain and instrumental broadening on the crystallite of the sample. The obtained C_{SCH} and C_{W-H} values are listed in Table 1.

Figure 2 shows the typical SEM images for $\text{La}_{0.8-x}\text{K}_x\text{Ba}_{0.05}\text{Sr}_{0.15}\text{MnO}_3$ samples in the secondary electron (SE) mode. It can be seen that there is an increasing trend of grain size for sample LKBS-0, LKBS-05, and LKBS-10. However, the grain sizes of LKBS-15 and LKBS-20 are smaller compared to LKBS-10. A similar case where larger grain size exists due to K^+ ion substitution has been reported by Thaljaoui et al. in $\text{Pr}_{0.6}\text{Sr}_{0.4-x}\text{K}_x\text{MnO}_3$ and Jerbi et al. in $\text{Pr}_{0.55}\text{Sr}_{0.45-x}\text{K}_x\text{MnO}_3$ [43,44]. Figure 2 also reveals the fact that the observed grain size varies between 0.4 μm and 1.92 μm .

Table 1. Results of Rietveld refinements obtained from powder diffraction pattern measured at room temperature for $\text{La}_{0.8-x}\text{K}_x\text{Ba}_{0.05}\text{Sr}_{0.15}\text{MnO}_3$ ($0 \leq x \leq 0.20$).

Structural Parameters	Sample Code				
	LKBS-0	LKBS-05	LKBS-10	LKBS-15	LKBS-20
$a = b$ (Å)	5.526	5.523	5.515	5.506	5.506
c (Å)	13.398	13.403	13.398	13.394	13.4
V (Å ³)	354.296	354.076	352.959	351.667	351.720
t_G	0.930	0.938	0.947	0.956	0.965
$\langle r_A \rangle$	1.243	1.260	1.276	1.293	1.310
σ^2 ($\times 10^{-3}$ Å ²)	3.833	8.237	12.083	15.371	18.101
C_{SCH} (nm)	38.57	61.75	58.66	58.37	58.86
C_{W-H} (nm)	133.32	211.07	156.61	172.08	173.88
R_{WP} (%)	9.681	9.220	9.303	8.623	9.035
χ^2 (%)	1.13	1.14	1.09	1.19	1.21

The difference in the crystallite size and the grain size observed from SEM measurement can be explained in terms of the method to determine the crystallite size of the sample. Zhou and Greer mentioned that the calculation of crystallite size from powder diffraction pattern will be in good agreement with the grain size observed from an electron microscope (either SEM or TEM) when the particle size of the sample is within the nanometer scale [45]. This is clearly not the case in the present work. Additionally, Uvarov and Popov also proved that in cases where two different crystal sizes exist—big crystals several microns in size and small crystals with a size of around 100 nm—the powder diffraction pattern would tend to detect only the presence of the small crystals [46]. Although the crystallite size of the samples reaches a resolution that can be detected through SEM measurement, it can be seen that the smallest grain size that can be seen in Figure 2 is 0.4 μm . This result indicates that each grain observed with SEM measurement comprises a secondary grain, which has aggregated into a single large grain. To determine this secondary grain, more sophisticated measurements, such as Atomic Force Microscopy (AFM) and Lateral Force Microscopy (LFM), will be needed [47].

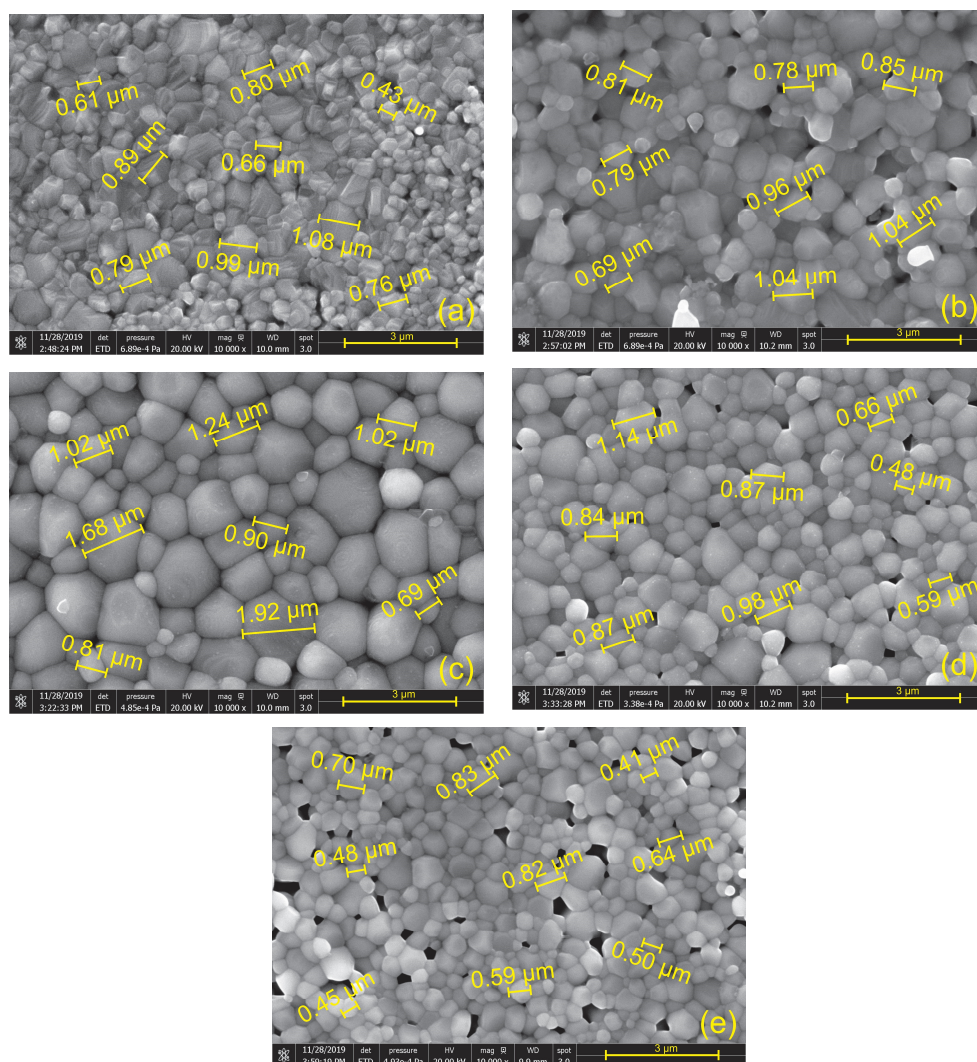


Figure 2. SEM micrograph of (a) LKBS-0, (b) LKBS-05, (c) LKBS-10, (d) LKBS-15, and (e) LKBS-20.

To confirm the existence of K^+ ion in the samples, EDX analysis together with elemental mapping analysis was performed. The elemental maps for each sample also demonstrate that each element is distributed evenly in the samples, hence proving that the sample has a high homogeneity. The elemental mapping of K^+ ion for LKBS-15 sample is brighter compared to LKBS-05. This proves that the concentration of K^+ ion in LKBS-15 sample is indeed higher compared to LKBS-05 sample. It is noteworthy to mention that the collection time in the elemental mapping of K^+ ion in LKBS-15 sample is shorter than LKBS-05. This result suggests that the concentration of K^+ ion in LKBS-15 sample is higher compared to the LKBS-05 sample, and the measurement result was not influenced by the collection time. Representative EDX spectra and elemental maps of LKBS-05 and LKBS-15 samples shown in Figure 3 ensure that K^+ ion was successfully substituted inside the samples. EDX quantitative analysis further confirms that K^+ has been successfully substituted in the samples. The results of EDX quantitative analysis for $La_{0.8-x}K_xBa_{0.05}Sr_{0.15}MnO_3$ ($0 \leq x \leq 0.20$) are listed in Table 2.

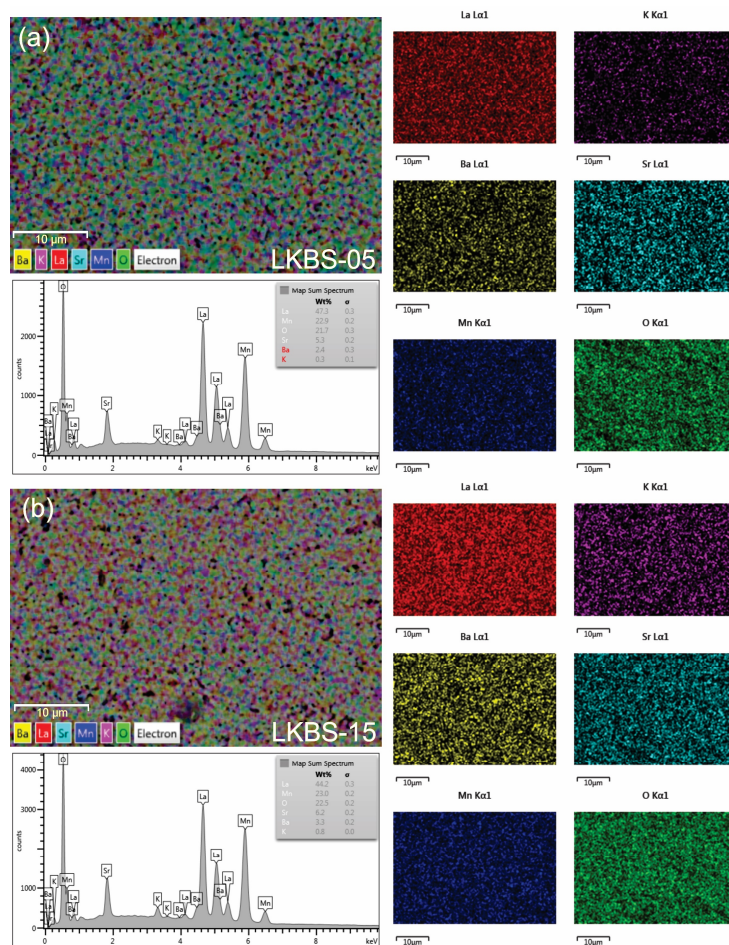


Figure 3. EDX spectra and elemental maps for six different elements of (a) LKBS-05 and (b) LKBS-15 samples.

Table 2. Weight percent of each element of $\text{La}_{0.8-x}\text{K}_x\text{Ba}_{0.05}\text{Sr}_{0.15}\text{MnO}_3$ ($0 \leq x \leq 0.20$) samples obtained from EDX quantitative analysis.

Elements	Weight Percent (%)				
	Sample Code				
	LKBS-0	LKBS-05	LKBS-10	LKBS-15	LKBS-20
O	22.49	22.09	22.89	22.64	21.62
Mn	22.11	22.91	23.23	23.02	23.3
K	0	0.51	0.75	0.86	0.9
Sr	5.29	5.1	6.21	6.65	6.43
Ba	2.48	2.7	2.07	3.21	3.46
La	47.63	46.7	44.85	43.62	44.29
Total	100	100	100	100	100

3.2. Magnetic Property Analysis

The temperature dependence of magnetization measured at an applied field of $\mu_0 H = 0.05$ T for $\text{La}_{0.8-x}\text{K}_x\text{Ba}_{0.05}\text{Sr}_{0.15}\text{MnO}_3$ samples (Figure 4a) shows that all samples exhibit a clear ferromagnetic-paramagnetic (FM-PM) transition. The Curie temperature (T_C) of $\text{La}_{0.8-x}\text{K}_x\text{Ba}_{0.05}\text{Sr}_{0.15}\text{MnO}_3$ samples were determined from the minimum value obtained from the first derivative of temperature dependence magnetization with respect to temperature (inset of Figure 4a). The results show that T_C increases monotonously with the increasing concentration of K^+ ion. The increasing trend of T_C can be interpreted in terms of the increase in Mn^{4+} concentration from 20%, for LKBS-0, to 40%, for LKBS-20. According

to the Zener theory of double exchange, the T_C of perovskite manganite-based material is expected to increase until it reaches a maximum value, which happens at a certain ratio of Mn^{3+}/Mn^{4+} [48]. According to several reports, the optimum value of Mn^{3+}/Mn^{4+} ratio was found to be around 7/3 or 2/1 [49–51]. The optimum value of Mn^{3+}/Mn^{4+} will favor the double exchange interaction between $Mn^{3+}-O^{2-}-Mn^{4+}$ ions while an excessive amount of Mn^{4+} will favor the superexchange interaction between $Mn^{4+}-O^{2-}-Mn^{4+}$ ions [52,53]. It is interesting to note that LKBS-20 sample with an expected Mn^{3+}/Mn^{4+} ratio of 3/2 has a higher T_C compared to LKBS-15 sample, which has an expected Mn^{3+}/Mn^{4+} ratio closer to optimum value. This can be interpreted in terms of electronic bandwidth (W) which can be calculated by the following equation [54]:

$$W \propto \frac{\cos \frac{1}{2} [\pi - \langle Mn - O - Mn \rangle]}{d_{<Mn-O>}^{3.5}} \quad (3)$$

where $d_{<Mn-O>}$ and $\langle Mn - O - Mn \rangle$ is the average bond length and bond angle, respectively. These two values can be obtained from Rietveld refinement analysis of powder diffraction pattern. A larger value of W implies that there is an enhancement in the exchange coupling of neighboring Mn ions, which results in higher T_C value [55]. The obtained $d_{<Mn-O>}$, $\langle Mn - O - Mn \rangle$, W , and T_C are listed in Table 3.

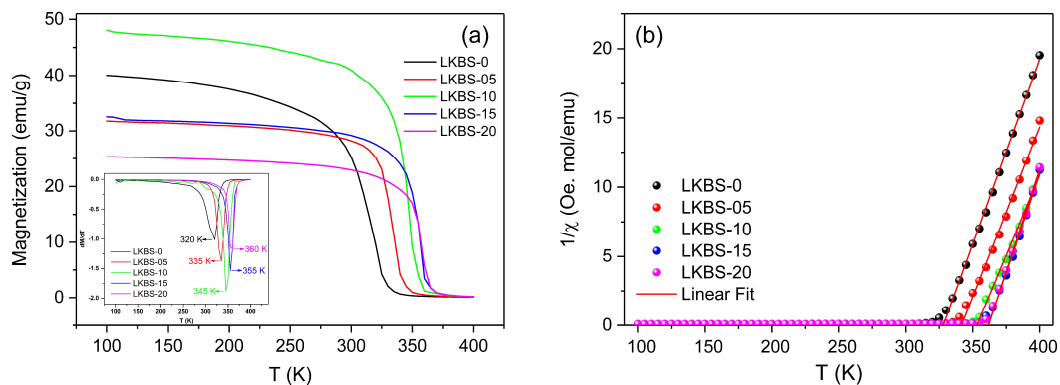


Figure 4. Temperature dependence of (a) magnetization and (b) inverse of magnetic susceptibility for $La_{0.8-x}K_xBa_{0.05}Sr_{0.15}MnO_3$ samples. Inset shows the first derivative of magnetization with respect to temperature.

The inverse of magnetic susceptibility of the $La_{0.8-x}K_xBa_{0.05}Sr_{0.15}MnO_3$ samples was calculated, and the result can be seen in Figure 4b. A linear trend in the high-temperature region suggests that the $La_{0.8-x}K_xBa_{0.05}Sr_{0.15}MnO_3$ samples follow the Curie–Weiss law, defined as [14]:

$$\chi = \frac{C}{T - \theta_{CW}} \quad (4)$$

here, χ is the magnetic susceptibility, C is the Curie constant and θ_{CW} is the Curie–Weiss temperature. The value of C can be obtained from the slopes of the graph while θ_{CW} can be obtained from the intercept of the slope with the temperature axis.

Fitting the high-temperature region of the inverse molar magnetic susceptibility with Curie–Weiss law will give valuable information regarding the magnetic property of the samples such as θ_{CW} and effective paramagnetic moment. The obtained θ_{CW} values of all samples were positive, which confirms the FM interactions between spins in the $La_{0.8-x}K_xBa_{0.05}Sr_{0.15}MnO_3$ samples [56]. The value of θ_{CW} is higher compared to the value T_C . This result suggests that there is a presence of short-range FM ordering in the temperature range slightly above T_C [57]. The presence of short-range ferromagnetic order can also be related to the presence of magnetic inhomogeneity in the samples [57].

The experimental effective paramagnetic moment (μ_{eff}^{exp}) can be calculated using the following equation [58]:

$$\mu_{eff}^{exp} = \sqrt{\frac{3k_B}{N_A}} \mu_B = \sqrt{8C} \mu_B \quad (5)$$

where $N_A = 6.023 \times 10^{23} \text{ mol}^{-1}$ is the Avogadro number, $k_B = 1.38016 \times 10^{-23} \text{ J}\cdot\text{K}^{-1}$ is the Boltzmann constant, and $\mu_B = 9.274 \times 10^{-21} \text{ emu}$ is the Bohr magneton. According to the chemical formula $\text{La}_{0.8-x}\text{K}_x\text{Ba}_{0.05}\text{Sr}_{0.15}\text{MnO}_3$, the theoretical effective paramagnetic moment (μ_{eff}^{theo}) can also be calculated using the following equation:

$$\mu_{eff}^{theo} = \sqrt{(0.8-x)[\mu_{eff}(\text{Mn}^{3+})]^2 + (0.2+x)[\mu_{eff}(\text{Mn}^{4+})]^2} \quad (6)$$

with $\mu_{eff}(\text{Mn}^{3+}) = 4.9 \mu_B$ and $\mu_{eff}(\text{Mn}^{4+}) = 3.87 \mu_B$ [59]. The obtained θ_{CW} , μ_{eff}^{exp} , and μ_{eff}^{theo} for $\text{La}_{0.8-x}\text{K}_x\text{Ba}_{0.05}\text{Sr}_{0.15}\text{MnO}_3$ samples are listed in Table 3. The difference between the value μ_{eff}^{exp} and μ_{eff}^{theo} for all $\text{La}_{0.8-x}\text{K}_x\text{Ba}_{0.05}\text{Sr}_{0.15}\text{MnO}_3$ samples suggest that there is an existence of FM clusters within PM phase [44].

Table 3. Magnetic parameters of $\text{La}_{0.8-x}\text{K}_x\text{Ba}_{0.05}\text{Sr}_{0.15}\text{MnO}_3$ samples.

Magnetic Parameters	Sample Code				
	LKBS-0	LKBS-05	LKBS-10	LKBS-15	LKBS-20
Mn^{3+} (expected)	0.8	0.75	0.7	0.65	0.6
Mn^{4+} (expected)	0.2	0.25	0.3	0.35	0.4
$\text{Mn}^{3+}/\text{Mn}^{4+}$	4/1	3/1	7/3	13/7	3/2
$d_{\text{Mn-O}}$ (Å)	1.97	1.97	1.96	1.97	1.95
$\angle \text{Mn-O-Mn}$ (°)	164.10	163.30	164.60	162.50	168.03
$W (\times 10^{-2})$	9.38	9.42	9.48	9.53	9.56
T_C (K)	320	335	345	355	360
θ_{CW}	328	341.6	353.1	361.5	361.8
$\mu_{eff}^{theo} (\mu_B)$	4.676	4.62	4.564	4.508	4.452
$\mu_{eff}^{exp} (\mu_B)$	5.471	5.710	5.88	5.301	5.21

3.3. Magnetocaloric Effect (MCE)

The isothermal magnetization curves at various temperatures near FM-PM transition under an applied magnetic field of up to $\mu_0 H = 5 \text{ T}$ are presented in Figure 5. The magnetization of all samples increases rapidly at temperatures below T_C , which implies a ferromagnetic state. On the other hand, the magnetization measured at temperatures higher than T_C shows a linear tendency. This can be related to the thermal effect that ruins the ferromagnetic order of the samples, thus implying a paramagnetic state.

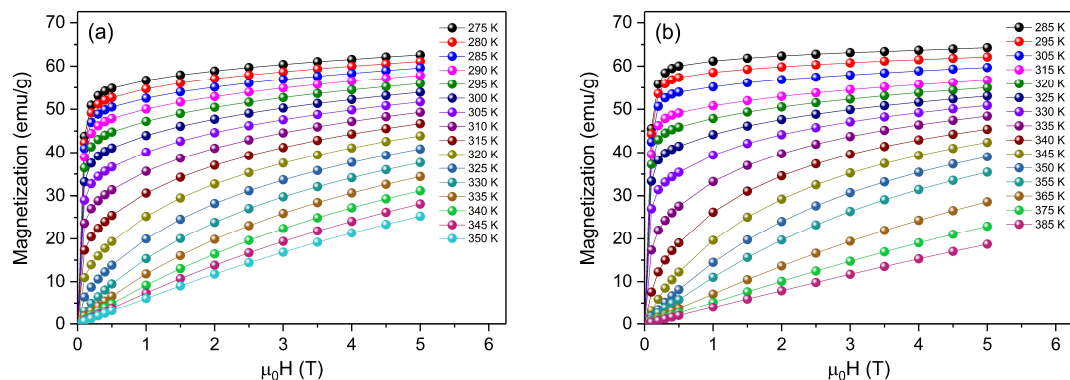


Figure 5. Cont.

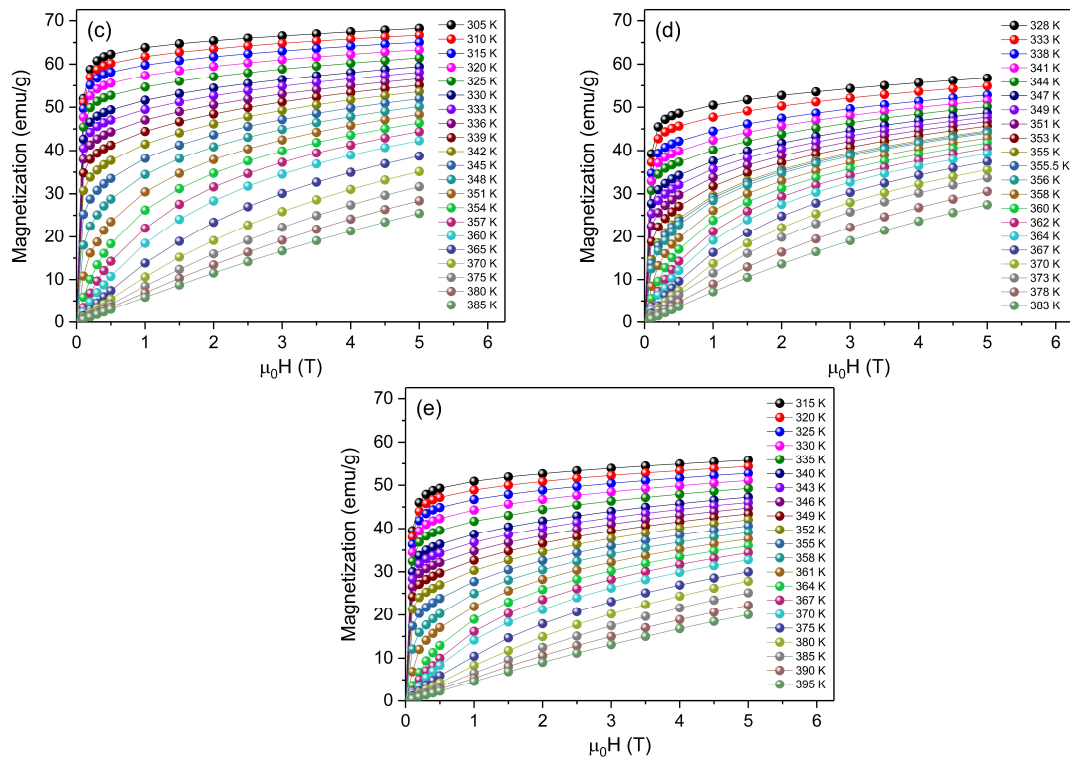


Figure 5. Isothermal magnetization curves taken at temperatures near the FM-PM transition for (a) LKBS-0, (b) LKBS-05, (c) LKBS-10, (d) LKBS-15, and (e) LKBS-20 samples.

The magnetic entropy change of $\text{La}_{0.8-x}\text{K}_x\text{Ba}_{0.05}\text{Sr}_{0.15}\text{MnO}_3$ samples can be calculated indirectly by calculating the magnetic entropy change ($\Delta S_M(T, \mu_0 H)$) from the measured isothermal magnetization. According to Maxwell's relation, the magnetic entropy change can be calculated from the following equation [60]:

$$\Delta S_M(T, \mu_0 H) = \int_0^{\mu_0 H} \left(\frac{\partial M(T, \mu_0 H)}{\partial T} \right) d(\mu_0 H) \quad (7)$$

The $-\Delta S_M$ values for the $\text{La}_{0.8-x}\text{K}_x\text{Ba}_{0.05}\text{Sr}_{0.15}\text{MnO}_3$ samples were calculated using Equation (7), and the results are presented in Figure 6. It can be noticed that the largest $-\Delta S_M$ value for all samples occurred around the T_C of each corresponding sample. The broad $-\Delta S_M$ curves of all samples suggest that each sample exhibits a second-order phase transition nature [61]. The maximum values of the magnetic entropy changes at 5 T ($-\Delta S_{M, \text{MAX}}$) were 4.21, 4.96, 5.18, 4.83, and 3.90 J/kg K for LKBS-0, LKBS-05, LKBS-10, LKBS-15, and LKBS-20, respectively. It is noteworthy to mention that according to Equation (7), the value of $-\Delta S_M$ is directly controlled by the first derivative of magnetization with respect to temperature (dM/dT). Referring to the dM/dT graph shown in the inset of Figure 4a, it can be seen that the slope reveals an increasing tendency until it reaches a maximum value, which belongs to the LKBS-10 sample. This fact is in a good agreement with the comparison of maximum $-\Delta S_M$ value at 5 T shown in Figure 6f which demonstrates that the largest $-\Delta S_M$ value is shown by the LKBS-10 sample.

Additionally, the evolution of $-\Delta S_M$ value is in accordance with the study of Hueso et al., which showed that in substituted LMO-based compounds the $-\Delta S_M$ value can also be affected by the grain size of the sample [62]. According to Hueso et al., the correlation between magnetocaloric property and the grain size of the sample is influenced by the presence of a magnetically disordered layer located at the outer part of the grain. This disordered layer will influence the magnetic phase transition at T_C resulting in a more gradual slope in the magnetic phase transition. The effect of the disordered layer is more pronounced in samples with smaller grain size, hence resulting in a smaller $-\Delta S_M$ value.

The consistency between the SEM micrograph (Figure 2) and the largest $-\Delta S_M$ value (Figure 6f) proves that the evolution of $-\Delta S_M$ value of $\text{La}_{0.8-x}\text{K}_x\text{Ba}_{0.05}\text{Sr}_{0.15}\text{MnO}_3$ samples is also influenced by the grain size of the sample.

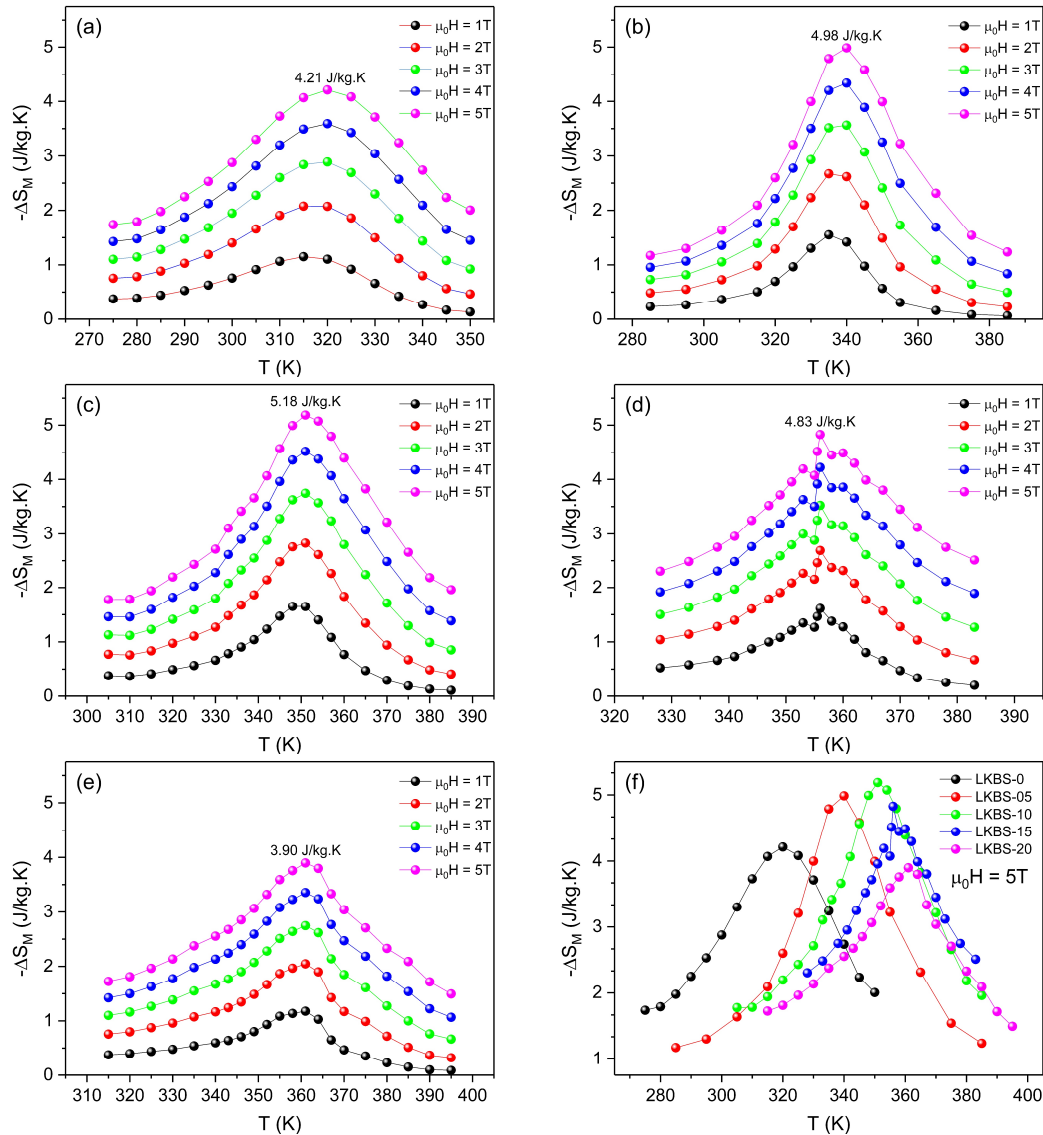


Figure 6. Magnetic entropy changes as a function of temperatures under an applied magnetic field ranging from 1 to 5 T for (a) LKBS-0, (b) LKBS-05, (c) LKBS-10, (d) LKBS-15, and (e) LKBS-20. (f) The comparison of the largest magnetic entropy changes of each sample obtained at 5 T.

It is clear that the $-\Delta S_M(T, \mu_0 H)$ graphs also show a maximum value at a certain temperature, which usually known as T_{peak} . Focusing the discussion on the $-\Delta S_M(T)$ at an applied magnetic field of 5 T, it can be seen that the value of T_{peak} increases monotonously with increasing K^+ ion concentration. The values of T_{peak} obtained in the present work were 320, 340, 351, 356, and 361 for LKBS-0, LKBS-05, LKBS-10, LKBS-15, and LKBS-20, respectively. The obtained T_{peak} values were slightly different compared to T_C , except for the LKBS-0 sample. Differences between T_{peak} and T_C are often found in substituted LMO-based compounds [51,55]. According to Franco et al., the difference between the value of T_C and T_{peak} in magnetocaloric compounds can be correlated with the critical behavior of the corresponding sample [63]. Furthermore, Franco et al. also mentioned that for magnetocaloric compounds with a critical behavior close to the mean-field model, the value of T_C can coincide with

T_{peak} [63]. The discussion regarding the critical behavior of $\text{La}_{0.8-x}\text{K}_x\text{Ba}_{0.05}\text{Sr}_{0.15}\text{MnO}_3$ samples will not be presented here, as this would require a different approach.

Another factor that holds a high degree of significance in the development of a magnetic refrigerator system is the cooling efficiency of the material, which is usually known as Relative Cooling Power (RCP). The RCP value can be calculated using the following equation [1]:

$$RCP = -\Delta S_{M, MAX} \times \delta T_{FWHM} \quad (8)$$

where $-\Delta S_{M, MAX}$ is the largest magnetic entropy change of the material and δT_{FWHM} is the full-width at half maximum (FWHM) of the corresponding magnetic entropy curve. The RCP for all samples at 5 T are 254, 219, 249, 301, and 173 J/kg for LKBS-0, LKBS-05, LKBS-10, LKBS-15, and LKBS-20, respectively. The large value of RCP obtained for all samples can also serve as a proof for the existence of second-order phase transition nature in the samples [61]. The obtained $-\Delta S_M$ and RCP value for all samples, as well as the values of other substituted LMO-based compounds are summarized in Table 4.

Table 4. Summary of $-\Delta S_{M, MAX}$ and RCP value of LKBS samples compared with several related compounds.

Sample	T_C (K)	$-\Delta S_{M, MAX}$ (J/kg·K)	RCP (J/kg)	$\Delta\mu_0 H$ (T)	Re
LKBS-0	320	1.15	166.1	1	this work
LKBS-05	335	1.55	130	1	this work
LKBS-10	345	1.65	132	1	this work
LKBS-15	355	1.61	103	1	this work
LKBS-20	360	1.18	112	1	this work
$\text{La}_{0.7}\text{Ba}_{0.2}\text{K}_{0.1}\text{MnO}_3$	311.5	0.74	-	1	[64]
$\text{La}_{0.75}\text{Ba}_{0.1}\text{K}_{0.15}\text{MnO}_3$	259	1.28	-	1	[29]
$\text{La}_{0.6}\text{Ba}_{0.2}\text{Sr}_{0.2}\text{MnO}_3$	354	2.26	-	1	[33]
LKBS-0	320	4.21	254	5	this work
LKBS-05	335	4.99	219	5	this work
LKBS-10	345	5.19	249	5	this work
LKBS-15	355	4.83	301	5	this work
LKBS-20	360	3.90	173	5	this work
$\text{La}_{0.8}(\text{Ag}_{0.25}\text{Sr}_{0.75})_{0.2}\text{MnO}_3$	336	3.4	275	5	[65]
$\text{La}_{0.7}\text{Sr}_{0.2}\text{Na}_{0.1}\text{MnO}_3$	340	4.07	118.4	5	[28]
$\text{La}_{0.67}\text{Ba}_{0.22}\text{Sr}_{0.11}\text{MnO}_3$	345	2.258	193	5	[66]

It is interesting to note that substitution by K^+ ion increases the $-\Delta S_{M, MAX}$ of the sample until it reaches the maximum value of 5.189 J/kg K, which corresponds to the LKBS-10 sample. Beyond this value, the $-\Delta S_{M, MAX}$ decreases with the increase in K^+ ion concentration. This result is in good agreement with the Zener theory of double exchange, which suggests that the physical properties of substituted LMO-based compounds are greatly influenced by $\text{Mn}^{3+}/\text{Mn}^{4+}$ ratio [48]. As mentioned earlier, substitution by K^+ ion changes the $\text{Mn}^{3+}/\text{Mn}^{4+}$ ratio from 4/1 for LKBS-0 sample to 3/2 for LKBS-20 sample. Within this range, LKBS-10 is expected to have an optimum $\text{Mn}^{3+}/\text{Mn}^{4+}$ ratio, which is equal to 7/3. Thus, it can be concluded that Zener theory of double exchange is proven to be reliable in explaining the $-\Delta S_{M, MAX}$ value of $\text{La}_{0.8-x}\text{K}_x\text{Ba}_{0.05}\text{Sr}_{0.15}\text{MnO}_3$ samples.

Previously, there have been several works that report the effect of K^+ ion substitution on the magnetic entropy change of LMO-based compounds. Roughly, the parental compound used in previous works can be classified into three different groups which are La-Cd-MnO₃, La-Ca-MnO₃, and La-Sr-MnO₃ [55,67–70]. In La-Cd-MnO₃ and La-Ca-MnO₃ compounds, substitution by K^+ ion increased the T_C of the samples, accompanied by a monotonous increase in the value of $-\Delta S_{M, MAX}$. According to the work of Dhahri et al., the T_C for $\text{La}_{0.8}\text{Cd}_{0.2-x}\text{K}_x\text{MnO}_3$ increases from 260 K to 282 K [69]. Meanwhile, Messaoui et al. reported that the T_C for $\text{La}_{0.78}\text{Cd}_{0.22-x}\text{K}_x\text{MnO}_3$ increased from 202 K to 326 K [68]. In line with the result of La-Cd-MnO₃ compound, a similar result was also found in the work of Koubaa et al. and Ben Rejeb et al. According to the work of Koubaa et al., the T_C of $\text{La}_{0.65}\text{Ca}_{0.35-x}\text{K}_x\text{MnO}_3$ increased from 248 to 310 K with K^+ ion concentration [55]. This increasing

trend of T_C was also followed by an increase of $-\Delta S_{M, MAX}$. An almost similar trend was also reported by Ben Rejeb et al., who also explored the effect of K^+ substitution on the $-\Delta S_{M, MAX}$ value of $La_{0.65}Ca_{0.35-x}K_xMnO_3$ compound. In their work, Ben Rejeb et al. even proved that substitution of the K^+ ion increased the values of T_C (from 248 K to 310 K and 275 K to 320 K for samples prepared using the solid-solid and sol-gel method, respectively) and $-\Delta S_{M, MAX}$, despite the difference in the sample preparation method [67]. It is important to note that in both of these groups, the value of $\langle r_A \rangle$ and σ^2 were increasing monotonously with K^+ concentration. This trend is in line with $La_{0.8-x}K_xBa_{0.05}Sr_{0.15}MnO_3$ samples. However, $La_{0.8-x}K_xBa_{0.05}Sr_{0.15}MnO_3$ samples do not reveal a similar trend for the $-\Delta S_{M, MAX}$ value. Furthermore, it is important to mention that the increase of T_C and $-\Delta S_{M, MAX}$ values for both La-Cd-MnO₃ and La-Ca-MnO₃ groups seems to disagree with the Zener theory of double exchange. In fact, the increasing value of $-\Delta S_{M, MAX}$ in La-Cd-MnO₃ and La-Ca-MnO₃ groups happened when the Mn^{4+} fractions were greater than the optimum values, which were 30% or 33%. In their work, Dhahri et al. suggested that the reason behind this result could be ascribed to the enhancement of spin-lattice coupling arising from a variation in the value of $d_{<Mn-O>}$ and $\langle Mn-O-Mn \rangle$ [69].

On the other hand, Cheikh-Rouhou Koubaa et al. studied the effect of K^+ ion substitution on the T_C and $-\Delta S_{M, MAX}$ value of $La_{0.7}Sr_{0.3-x}K_xMnO_3$ [70]. According to their work, the T_C of $La_{0.7}Sr_{0.3-x}K_xMnO_3$ decreased monotonously with an increase in the concentration of K^+ fraction from 365 K to 328 K, from $x = 0$ to $x = 0.2$, respectively. Additionally, the increasing concentration of K^+ ion in $La_{0.7}Sr_{0.3-x}K_xMnO_3$ further reduced the value of $-\Delta S_{M, MAX}$, with a minimum value of 1.2 J/kg K for $x = 0.15$. In their work, Cheikh-Rouhou Koubaa et al. suggested that the reduction in T_C and $-\Delta S_{M, MAX}$ value could be ascribed to the weakening of the double exchange mechanism due to the increase of the Mn^{4+} fraction, which is expected to be greater than 30%. This result also suggests that the behavior of T_C and $-\Delta S_{M, MAX}$ of La-Sr-MnO₃ which have been substituted by K^+ ion is in good agreement with the Zener theory of double exchange.

Summarizing the points mentioned above, it seems that the Zener theory of double exchange is less prominent in LMO-based compounds composed of at least one ion with small ionic radii such as Ca^{2+} and Cd^{2+} ions, with an ionic radius of 1.18 Å and 1.03 Å [26]. In such a compound, other factors such as $\langle r_A \rangle$, σ^2 , and spin-lattice coupling from $d_{<Mn-O>}$ and $\langle Mn-O-Mn \rangle$ apparently outperform the double exchange mechanism. On the other hand, the Zener theory of double exchange seems to be more prominent compared to other factors if the LMO-based compounds is composed of at least one ion with large ionic radii such as Sr^{2+} ion with ionic radius of 1.31 Å [26]. Returning to the current topic, it is clear that $La_{0.8-x}K_xBa_{0.05}Sr_{0.15}MnO_3$ samples are composed of ions with large ionic radii. The ionic radii of each A-site ion in the $La_{0.8-x}K_xBa_{0.05}Sr_{0.15}MnO_3$ samples are 1.22 Å, 1.31 Å, 1.47 Å, and 1.55 Å for La^{3+} , Sr^{2+} , Ba^{2+} , and K^+ ion, respectively [26]. Hence, it is expected that in $La_{0.8-x}K_xBa_{0.05}Sr_{0.15}MnO_3$ samples, the Zener theory of double exchange will become a prominent factor in controlling the $-\Delta S_{M, MAX}$ value of $La_{0.8-x}K_xBa_{0.05}Sr_{0.15}MnO_3$ samples. Comparisons of T_C and $-\Delta S_{M, MAX}$ values for $La_{0.8-x}K_xBa_{0.05}Sr_{0.15}MnO_3$ samples in graphical form, as well as the comparison with $\langle r_A \rangle$ and σ^2 value, are presented in graphical form in Figure 7.

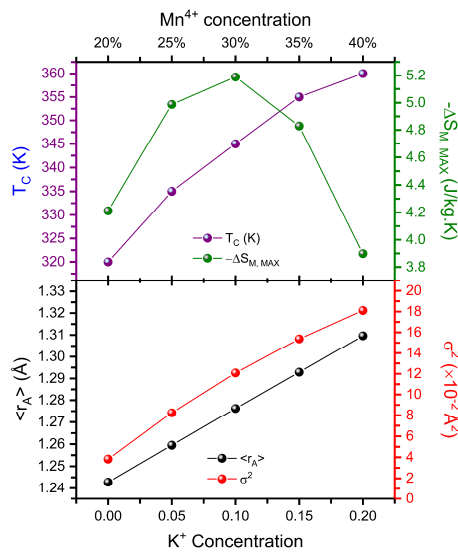


Figure 7. Comparison between T_C and $-\Delta S_{M, MAX}$ with $\langle r_A \rangle$ and σ^2 value for $\text{La}_{0.8-x}\text{K}_x\text{Ba}_{0.05}\text{Sr}_{0.15}\text{MnO}_3$ samples.

To support the previous argument whereby all of the $\text{La}_{0.8-x}\text{K}_x\text{Ba}_{0.05}\text{Sr}_{0.15}\text{MnO}_3$ samples belong to the second-order phase transition type, a universal master curve based on the phenomenological approach proposed by Franco et al. was constructed [71]. According to Franco et al., the measured $-\Delta S_M$ as a function of temperature under different applied magnetic fields will coincide with a single master curve for a material with second-order phase transition. In detail, this approach was carried out by normalizing magnetic entropy change to its maximum value for each applied magnetic field. Additionally, the temperature axis needs to be modified by rescaling the temperature with new variable θ , defined by the following equation:

$$\begin{aligned} \theta &= -(T - T_C) / (T_{r1} - T_C) \text{ for } T \leq T_C \\ \theta &= (T - T_C) / (T_{r2} - T_C) \text{ for } T > T_C \end{aligned} \quad (9)$$

where T_{r1} and T_{r2} are references temperature taken when the value of ΔS_M is approximately half of the maximum value. The universal master curve for all $\text{La}_{0.8-x}\text{K}_x\text{Ba}_{0.05}\text{Sr}_{0.15}\text{MnO}_3$ samples is shown in Figure 8. It is obvious that the universal master curve of all $\text{La}_{0.8-x}\text{K}_x\text{Ba}_{0.05}\text{Sr}_{0.15}\text{MnO}_3$ samples coincides into a single curve. This result confirms that all $\text{La}_{0.8-x}\text{K}_x\text{Ba}_{0.05}\text{Sr}_{0.15}\text{MnO}_3$ samples belong to the second-order phase transition.

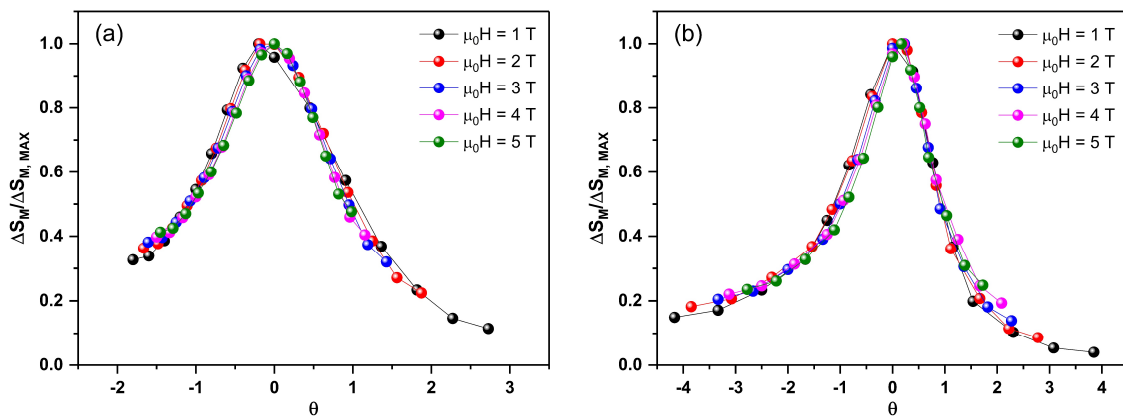


Figure 8. Cont.

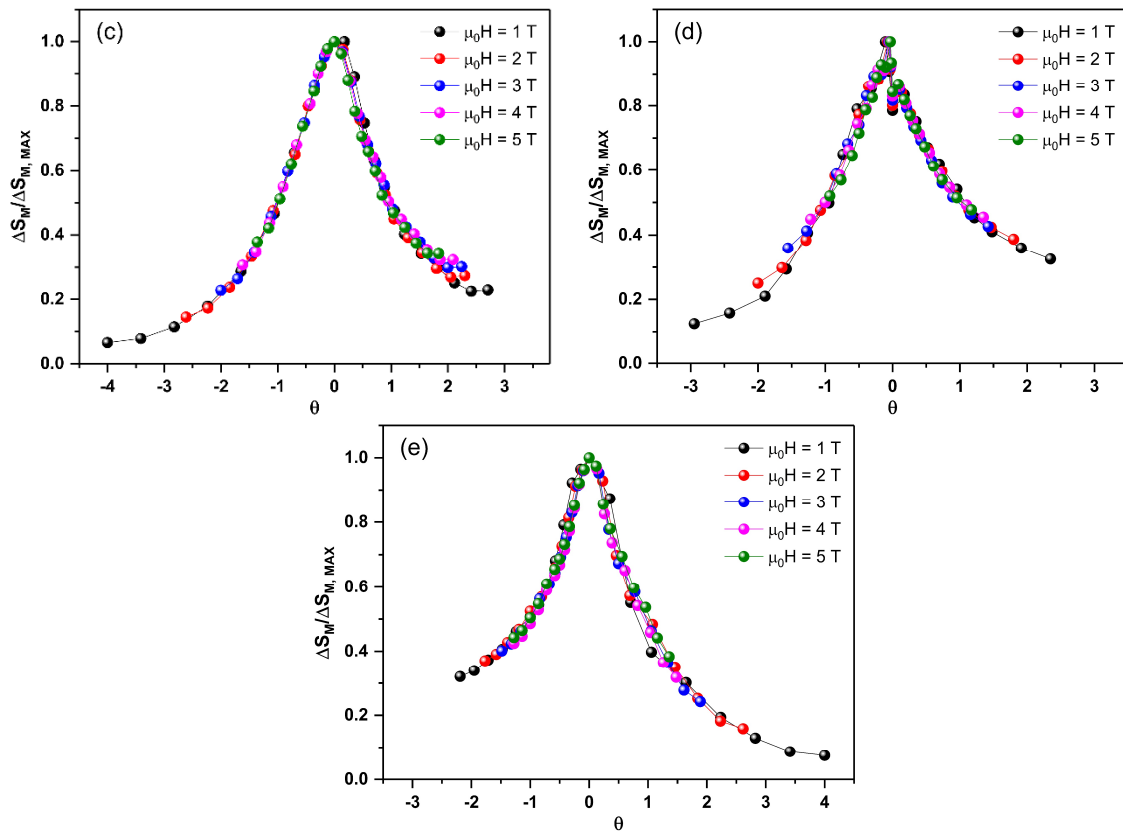


Figure 8. The universal master curve for (a) LKBS-0, (b) LKBS-05, (c) LKBS-10, (d) LKBS-15, and (e) LKBS-20 samples.

4. Conclusions

To summarize, the effect of K^+ substitution on the crystal structure and magnetic property, as well as the magnetic entropy change of $La_{0.8-x}K_xBa_{0.05}Sr_{0.15}MnO_3$ ($0 \leq x \leq 0.20$), was investigated. All samples were crystallized in a rhombohedral structure with R-3c space group. Magnetization investigation by means of the Field Cooling (FC) method revealed that all samples exhibited a clear ferromagnetic (FM) to paramagnetic (PM) transition at the Curie temperature (T_C). Substitution by K^+ ion increases the T_C of $La_{0.8-x}K_xBa_{0.05}Sr_{0.15}MnO_3$ ($0 \leq x \leq 0.20$) from 320 K to 360 K. Moreover, the magnetic entropy change ($-\Delta S_M$) under an applied magnetic field of 5 T also increased to 4.21, 4.99, 5.19, 4.83, and 3.90 J/kg K for $x = 0, 0.05, 0.1, 0.15$, and 0.2 , respectively. The fluctuation in $-\Delta S_M$ value can be interpreted in terms of variation in Mn^{3+}/Mn^{4+} ratio due to the increasing population of Mn^{4+} ion as K^+ concentration increases. The smallest relative cooling power (RCP) was 173 J/kg for LKBS-20 sample and the largest RCP was 301 J/kg for LKBS-15 sample. The obtained values of T_C , $-\Delta S_M$ and RCP value of $La_{0.8-x}K_xBa_{0.05}Sr_{0.15}MnO_3$ suggests that it can be considered as a good candidate for magnetic refrigeration system above room temperature.

Author Contributions: Conceptualization, D.S.R. and B.K.; methodology, D.S.R.; validation, B.K., D.R.M. and H.T.; formal analysis, D.S.R. and D.R.M.; investigation, D.S.R.; data curation, K.W.; writing—original draft preparation, D.S.R.; writing—review and editing, B.K., D.R.M. and H.T.; supervision, B.K.; project administration, B.K.; funding acquisition, B.K. All authors have read and agreed to the published version of the manuscript.

Funding: This research was funded by The Ministry of Research, Technology, and Higher Education (Kemenristek Dikti) with PDUPT 2019 grant number [NKB-1590/UN2.R3.1/HKP.05.00/2019]

Conflicts of Interest: The authors declare no conflict of interest.

References

- Gschneidner, K.A.; Pecharsky, V.K. Magnetocaloric materials. *Annu. Rev. Mater. Sci.* **2000**, *30*, 387–429. [\[CrossRef\]](#)
- Tishin, A.M.; Spichkin, Y.I. *The Magnetocaloric Effect and Its Applications*; IOP Publishing Ltd: Bristol, UK, 2016; Volume 6, ISBN 9781420033373.
- Pecharsky, V.K.; Gschneidner Jr, K.A. Magnetocaloric effect and magnetic refrigeration. *J. Magn. Magn. Mater.* **1999**, *200*, 44–56. [\[CrossRef\]](#)
- Gschneidner, K.A., Jr.; Pecharsky, V.K.; Tsokol, A.O. Recent developments in magnetocaloric materials. *Reports Prog. Phys.* **2005**, *68*, 1479–1539. [\[CrossRef\]](#)
- Pecharsky, V.K.; Gschneidner, K.A. Giant magnetocaloric effect in $\text{Gd}_5(\text{Si}_2\text{Ge}_2)$. *Phys. Rev. Lett.* **1997**, *78*, 4494–4497. [\[CrossRef\]](#)
- Wada, H.; Tanabe, Y. Giant magnetocaloric effect of $\text{MnAs}_{1-x}\text{Sb}_x$. *Appl. Phys. Lett.* **2001**, *79*, 3302–3304. [\[CrossRef\]](#)
- Fukamichi, K.; Fujita, A.; Fujieda, S. Large magnetocaloric effects and thermal transport properties of $\text{La}(\text{FeSi})_{13}$ and their hydrides. *J. Alloys Compd.* **2006**, *408–412*, 307–312. [\[CrossRef\]](#)
- Phan, M.-H.; Yu, S.-C. Review of the magnetocaloric effect in manganite materials. *J. Magn. Magn. Mater.* **2007**, *308*, 325–340. [\[CrossRef\]](#)
- Maignan, A.; Simon, C.; Caignaert, V.; Raveau, B. Colossal magnetoresistance properties of the manganese perovskites. $\text{La}_{0.7-x}\text{Y}_x\text{Ca}_{0.3}\text{MnO}_{3-\delta}$. *J. Appl. Phys.* **1996**, *79*, 7891–7895. [\[CrossRef\]](#)
- Zhang, S.; Cao, Q. Electromagnetic and microwave absorption performance of some transition metal doped $\text{La}_{0.7}\text{Sr}_{0.3}\text{Mn}_{1-x}\text{TM}_x\text{O}_{3\pm\delta}$ (TM = Fe, Co or Ni). *Mater. Sci. Eng. B* **2012**, *177*, 678–684. [\[CrossRef\]](#)
- Jiang, S.P. Development of lanthanum strontium manganite perovskite cathode materials of solid oxide fuel cells: A review. *J. Mater. Sci.* **2008**, *43*, 6799–6833. [\[CrossRef\]](#)
- Yamamoto, T.; Noguchi, S.; Yasumoto, K.; Itoh, H.; Takeda, Y. Chemical Stability of Lanthanum Manganite and Reactivity with Ytria-Stabilized Zirconia. In *Solid State Ionics*; World Scientific: Toh Tuck Link, Singapore, 2004; Volume 3, pp. 281–288.
- Turky, A.O.; Rashad, M.M.; Hassan, A.M.; Elnaggar, E.M.; Bechelany, M. Optical, electrical and magnetic properties of lanthanum strontium manganite $\text{La}_{1-x}\text{Sr}_x\text{MnO}_3$ synthesized through the citrate combustion method. *Phys. Chem. Chem. Phys.* **2017**, *19*, 6878–6886. [\[CrossRef\]](#) [\[PubMed\]](#)
- Ezaami, A.; Sellami-Jmal, E.; Chaaba, I.; Cheikhrouhou-Koubaa, W.; Cheikhrouhou, A.; Hlil, E.K. Effect of elaborating method on magnetocaloric properties of $\text{La}_{0.7}\text{Ca}_{0.2}\text{Ba}_{0.1}\text{MnO}_3$ manganite. *J. Alloys Compd.* **2016**, *685*, 710–719. [\[CrossRef\]](#)
- Moradi, J.; Ghazi, M.E.; Ehsani, M.H.; Kameli, P. Structural and magnetic characterization of $\text{La}_{0.8}\text{Sr}_{0.2}\text{MnO}_3$ nanoparticles prepared via a facile microwave-assisted method. *J. Solid State Chem.* **2014**, *215*, 1–7. [\[CrossRef\]](#)
- Xu, Z.; Wei, C.; Ai-Jun, L.; Li-Mei, M.; Yun, Z. Structural, Magnetic and Magnetocaloric Properties of La-deficient $\text{La}_{0.77-x}\text{Sr}_x\text{Ca}_{0.2}\text{MnO}_3$ Perovskites. *Chinese Phys. Lett.* **2009**, *26*, 087401. [\[CrossRef\]](#)
- Demin, R.V.; Koroleva, L.I. Influence of the magnetic two-phase state on the magnetocaloric effect in manganites. *Phys. Lett. A* **2003**, *317*, 140–143. [\[CrossRef\]](#)
- Terashita, H.; Garbe, J.J.; Neumeier, J.J. Compositional dependence of the magnetocaloric effect in $\text{La}_{1-x}\text{Ca}_x\text{MnO}_3$ ($0 \leq x \leq 0.52$). *Phys. Rev. B* **2004**, *70*, 094403. [\[CrossRef\]](#)
- Szewczyk, A.; Gutowska, M.; Dabrowski, B.; Plackowski, T.; Danilova, N.P.; Gaidukov, Y.P. Specific heat anomalies in $\text{La}_{1-x}\text{Sr}_x\text{MnO}_3$ ($0.12 \leq x \leq 0.2$). *Phys. Rev. B* **2005**, *71*, 224432. [\[CrossRef\]](#)
- Jeddi, M.; Gharsallah, H.; Bekri, M.; Dhahri, E.; Hlil, E.K. Structural, magnetic, critical behavior and phenomenological investigation of magnetocaloric properties of $\text{La}_{0.6}\text{Ca}_{0.4-x}\text{Sr}_x\text{MnO}_3$ perovskite. *J. Mater. Sci. Mater. Electron.* **2019**, *30*, 14430–14444. [\[CrossRef\]](#)
- Sffir Debbebi, I.; Cheikhrouhou-Koubaa, W.; Cheikhrouhou, A.; Hlil, E.K. Structural, magnetic and magnetocaloric investigation of $\text{La}_{0.7-x}\text{Dy}_x\text{Ca}_{0.3}\text{MnO}_3$ ($x = 0.00, 0.01$ and 0.03) manganite. *J. Mater. Sci. Mater. Electron.* **2017**, *28*, 16965–16972. [\[CrossRef\]](#)
- Zarifi, M.; Kameli, P.; Raoufi, T.; Ghotbi Varzaneh, A.; Salazar, D.; Nouraddini, M.I.; Kotsedi, L.; Maaza, M. Direct and indirect measurement of the magnetocaloric effect in the $\text{La}_{0.5}\text{Ca}_{0.5-x}\text{Pb}_x\text{MnO}_3$ ($0 \leq x \leq 0.2$) manganites. *J. Magn. Magn. Mater.* **2020**, *494*, 165734. [\[CrossRef\]](#)

23. Tang, T.; Gu, K.; Cao, Q.; Wang, D.; Zhang, S.; Du, Y. Magnetocaloric properties of Ag-substituted perovskite-type manganites. *J. Magn. Magn. Mater.* **2000**, *222*, 110–114. [\[CrossRef\]](#)
24. Thaljaoui, R.; Boujelben, W.; Pekała, K.; Pekała, M.; Cheikhrouhou-Koubaa, W.; Cheikhrouhou, A. Magnetocaloric study of monovalent-doped manganites $\text{Pr}_{0.6}\text{Sr}_{0.4-x}\text{Na}_x\text{MnO}_3$ ($x = 0-0.2$). *J. Mater. Sci.* **2013**, *48*, 3894–3903. [\[CrossRef\]](#)
25. Varshney, D.; Dodiya, N. Metallic and semi-conducting resistivity behaviour of $\text{La}_{0.7}\text{Ca}_{0.3-x}\text{K}_x\text{MnO}_3$ ($x = 0.05, 0.1$) manganites. *J. Theor. Appl. Phys.* **2015**, *9*, 45–58. [\[CrossRef\]](#)
26. Shannon, R.D. Revised effective ionic radii and systematic studies of interatomic distances in halides and chalcogenides. *Acta Crystallogr. Sect. A* **1976**, *32*, 751–767. [\[CrossRef\]](#)
27. Ayadi, F.; Saadaoui, F.; Cheikhrouhou-Koubaa, W.; Koubaa, M.; Cheikhrouhou, A.; Sicard, L.; Ammar, S. Effect of monovalent doping on the physical properties of $\text{La}_{0.7}\text{Sr}_{0.3}\text{MnO}_3$ compound synthesized using sol-gel technique. *IOP Conf. Ser. Mater. Sci. Eng.* **2012**, *28*, 012054. [\[CrossRef\]](#)
28. Cheikh-Rouhou Koubaa, W.; Koubaa, M.; Cheikhrouhou, A. Effect of Monovalent Doping on the Structural, Magnetic and Magnetocaloric Properties in $\text{La}_{0.7}\text{M}_{0.2}\text{M}'_{0.1}\text{MnO}_3$ Manganese Oxides ($\text{M} = \text{Sr}, \text{Ba}$ and $\text{M}' = \text{Na}, \text{Ag}, \text{K}$). *Phys. Procedia* **2009**, *2*, 989–996. [\[CrossRef\]](#)
29. Koubaa, M.; Koubaa, W.C.-R.; Cheikhrouhou, A. Magnetocaloric effect and magnetic properties of $\text{La}_{0.75}\text{Ba}_{0.1}\text{M}_{0.15}\text{MnO}_3$ ($\text{M} = \text{Na}, \text{Ag}$ and K) perovskite manganites. *J. Alloys Compd.* **2009**, *479*, 65–70. [\[CrossRef\]](#)
30. Regaieg, Y.; Koubaa, M.; Koubaa, W.C.; Cheikhrouhou, A.; Sicard, L.; Ammar-Merah, S.; Herbst, F. Structure and magnetocaloric properties of $\text{La}_{0.8}\text{Ag}_{0.2-x}\text{K}_x\text{MnO}_3$ perovskite manganites. *Mater. Chem. Phys.* **2012**, *132*, 839–845. [\[CrossRef\]](#)
31. Koubaa, M.; Cheikhrouhou Koubaa, W.; Cheikhrouhou, A. Magnetic and magnetocaloric properties of monovalent substituted $\text{La}_{0.65}\text{M}_{0.3}\text{M}'_{0.05}\text{MnO}_3$ ($\text{M} = \text{Ba}, \text{Ca}$ and $\text{M}' = \text{Na}, \text{Ag}, \text{K}$) perovskite manganites. *Phys. Procedia* **2009**, *2*, 997–1004. [\[CrossRef\]](#)
32. Zhong, W.; Au, C.-T.; Du, Y.-W. Review of magnetocaloric effect in perovskite-type oxides. *Chin. Phys. B* **2013**, *22*, 057501. [\[CrossRef\]](#)
33. Phan, M.H.; Tian, S.B.; Hoang, D.Q.; Yu, S.C.; Nguyen, C.; Ulyanov, A.N. Large magnetic-entropy change above 300 K in CMR materials. *J. Magn. Magn. Mater.* **2003**, *258–259*, 309–311. [\[CrossRef\]](#)
34. Banik, S.; Das, I. Effect of A-site ionic disorder on magnetocaloric properties in large band width manganite systems. *J. Alloys Compd.* **2018**, *742*, 248–255. [\[CrossRef\]](#)
35. Pham, Y.; Manh, T.V.; Thanh, T.D.; Yang, D.S.; Yu, S.C.; Kim, D.H. Magnetic and table-like magnetocaloric properties of polycrystalline $\text{Pr}_{0.7}\text{Ba}_{0.1}\text{Sr}_{0.2}\text{MnO}_3$. *J. Electron. Mater.* **2019**, *48*, 6583–6590. [\[CrossRef\]](#)
36. Li, Y.; Xue, L.; Fan, L.; Yan, Y. The effect of citric acid to metal nitrates molar ratio on sol-gel combustion synthesis of nanocrystalline LaMnO_3 powders. *J. Alloys Compd.* **2009**, *478*, 493–497. [\[CrossRef\]](#)
37. Xi, S.; Lu, W.; Sun, Y. Magnetic properties and magnetocaloric effect of $\text{La}_{0.8}\text{Ca}_{0.2}\text{MnO}_3$ nanoparticles tuned by particle size. *J. Appl. Phys.* **2012**, *111*, 063922. [\[CrossRef\]](#)
38. Toby, B.H.; Von Dreele, R.B. GSAS-II: The genesis of a modern open-source all purpose crystallography software package. *J. Appl. Crystallogr.* **2013**, *46*, 544–549. [\[CrossRef\]](#)
39. Shaikh, M.W.; Varshney, D. Structural properties and electrical resistivity behaviour of $\text{La}_{1-x}\text{K}_x\text{MnO}_3$ ($x = 0.1, 0.125$ and 0.15) manganites. *Mater. Chem. Phys.* **2012**, *134*, 886–898. [\[CrossRef\]](#)
40. Chebaane, M.; Bellouz, R.; Oumezzine, M.; Hlil, E.K.; Fouzri, A. Copper-doped lanthanum manganite $\text{La}_{0.65}\text{Ce}_{0.05}\text{Sr}_{0.3}\text{Mn}_{1-x}\text{Cu}_x\text{O}_3$ influence on structural, magnetic and magnetocaloric effects. *RSC Adv.* **2018**, *8*, 7186–7195. [\[CrossRef\]](#)
41. Holzwarth, U.; Gibson, N. The Scherrer equation versus the “Debye-Scherrer equation”. *Nat. Nanotechnol.* **2011**, *6*, 534. [\[CrossRef\]](#)
42. Williamson, G.; Hall, W. X-ray line broadening from fcc aluminium and wolfram. *Acta Metall.* **1953**, *1*, 22–31. [\[CrossRef\]](#)
43. Thaljaoui, R.; Boujelben, W.; Pekała, M.; Pekała, K.; Fagnard, J.-F.; Vanderbemden, P.; Donten, M.; Cheikhrouhou, A. Magnetocaloric effect of monovalent K doped manganites $\text{Pr}_{0.6}\text{Sr}_{0.4-x}\text{K}_x\text{MnO}_3$ ($x = 0$ to 0.2). *J. Magn. Magn. Mater.* **2014**, *352*, 6–12. [\[CrossRef\]](#)
44. Jerbi, A.; Thaljaoui, R.; Krichene, A.; Boujelben, W. Structural, magnetic and electrical study of polycrystalline $\text{Pr}_{0.55}\text{Sr}_{0.45-x}\text{K}_x\text{MnO}_3$ ($x = 0, 0.05$ and 0.1). *Phys. B Condens. Matter* **2014**, *442*, 21–28. [\[CrossRef\]](#)

45. Zhou, W.; Greer, H.F. What can electron microscopy tell us beyond crystal structures? *Eur. J. Inorg. Chem.* **2016**, *2016*, 941–950. [\[CrossRef\]](#)
46. Uvarov, V.; Popov, I. Metrological characterization of X-ray diffraction methods at different acquisition geometries for determination of crystallite size in nano-scale materials. *Mater. Charact.* **2013**, *85*, 111–123. [\[CrossRef\]](#)
47. Solanki, P.S.; Doshi, R.R.; Thaker, C.M.; Pandya, S.; Ganesan, V.; Kuberkar, D.G. Transport and Magnetotransport Studies on Sol–Gel Grown Nanostructured $\text{La}_{0.7}\text{Pb}_{0.3}\text{MnO}_3$ Manganites. *J. Nanosci. Nanotechnol.* **2009**, *9*, 5681–5686. [\[CrossRef\]](#) [\[PubMed\]](#)
48. Zener, C. Interaction between the d-shells in the transition metals. II. Ferromagnetic compounds of manganese with Perovskite structure. *Phys. Rev.* **1951**, *82*, 403–405. [\[CrossRef\]](#)
49. Guo, Z.B.; Du, Y.W.; Zhu, J.S.; Huang, H.; Ding, W.P.; Feng, D. Large magnetic entropy change in perovskite-type manganese oxides. *Phys. Rev. Lett.* **1997**, *78*, 1142–1145. [\[CrossRef\]](#)
50. Chau, N.; Nhat, H.N.; Luong, N.H.; Minh, D.L.; Tho, N.D.; Chau, N.N. Structure, magnetic, magnetocaloric and magnetoresistance properties of $\text{La}_{1-x}\text{Pb}_x\text{MnO}_3$ perovskite. *Phys. B Condens. Matter* **2003**, *327*, 270–278. [\[CrossRef\]](#)
51. Das, S.; Dey, T.K. Magnetic entropy change in polycrystalline $\text{La}_{1-x}\text{K}_x\text{MnO}_3$ perovskites. *J. Alloys Compd.* **2007**, *440*, 30–35. [\[CrossRef\]](#)
52. Izyumov, Y.A.; Skryabin, Y.N. Double exchange model and the unique properties of the manganites. *Uspekhi Fiz. Nauk* **2001**, *171*, 147–148. [\[CrossRef\]](#)
53. Abdelmoula, N.; Cheikh-Rouhou, A.; Reversat, L. Structural, magnetic and magnetoresistive properties of $\text{La}_{0.7}\text{Sr}_{0.3-x}\text{Na}_x\text{MnO}_3$ manganites. *J. Phys. Condens. Matter* **2001**, *13*, 449–458. [\[CrossRef\]](#)
54. Radaelli, P.; Iannone, G.; Marezio, M. Structural effects on the magnetic and transport properties of perovskite $\text{A}_{1-x}\text{A}'_x\text{MnO}_3$ ($x = 0.25, 0.30$). *Phys. Rev. B* **1997**, *56*, 8265–8276. [\[CrossRef\]](#)
55. Koubaa, M.; Cheikhrouhou-Koubaa, W.; Cheikhrouhou, A. Effect of K doping on the physical properties of $\text{La}_{0.65}\text{Ca}_{0.35-x}\text{K}_x\text{MnO}_3$ ($0 \leq x \leq 0.2$) perovskite manganites. *J. Phys. Chem. Solids* **2009**, *70*, 326–333. [\[CrossRef\]](#)
56. Ben Khelifa, H.; Othmani, S.; Chaaba, I.; Tarhouni, S.; Cheikhrouhou-Koubaa, W.; Koubaa, M.; Cheikhrouhou, A.; Hlil, E.K. Effect of K-doping on the structural, magnetic and magnetocaloric properties of $\text{Pr}_{0.8}\text{Na}_{0.2-x}\text{K}_x\text{MnO}_3$ ($0 \leq x \leq 0.15$) manganites. *J. Alloys Compd.* **2016**, *680*, 388–396. [\[CrossRef\]](#)
57. Zaidi, A.; Cherif, K.; Dhahri, J.; Hlil, E.K.; Zaidi, M.; Alharbi, T. Influence of Na-doping in $\text{La}_{0.67}\text{Pb}_{0.33-x}\text{Na}_x\text{MnO}_3$ ($0 \leq x \leq 0.15$) on its structural, magnetic and magneto-electrical properties. *J. Alloys Compd.* **2015**, *650*, 210–216. [\[CrossRef\]](#)
58. Modi, A.; Gaur, N.K. Effect of Sm substitution on magnetic and magnetocaloric properties of $\text{La}_{0.7-x}\text{Sm}_x\text{Ba}_{0.3}\text{MnO}_3$ ($0 \leq x \leq 0.2$) compounds. *J. Magn. Magn. Mater.* **2017**, *441*, 217–221. [\[CrossRef\]](#)
59. Cullity, B.D.; Graham, C.D. *Introduction to Magnetic Materials*; John Wiley & Sons: Hoboken, NJ, USA, 2011.
60. Bohigas, X.; Tejada, J.; Marínez-Sarrión, M.; Tripp, S.; Black, R. Magnetic and calorimetric measurements on the magnetocaloric effect in $\text{La}_{0.6}\text{Ca}_{0.4}\text{MnO}_3$. *J. Magn. Magn. Mater.* **2000**, *208*, 85–92. [\[CrossRef\]](#)
61. Bouzaïene, E.; Dhahri, A.H.; Dhahri, J.; Hlil, E.K.; Bajahzar, A. Effect of A-site-substitution on structural, magnetic and magnetocaloric properties in $\text{La}_{0.7}\text{Sr}_{0.3}\text{Mn}_{0.9}\text{Cu}_{0.1}\text{O}_3$ manganite. *J. Magn. Magn. Mater.* **2019**, *491*, 165540. [\[CrossRef\]](#)
62. Hueso, L.E.; Sande, P.; Miguéns, D.R.; Rivas, J.; Rivadulla, F.; López-Quintela, M.A. Tuning of the magnetocaloric effect in $\text{La}_{0.67}\text{Ca}_{0.33}\text{MnO}_{3-\delta}$ nanoparticles synthesized by sol-gel techniques. *J. Appl. Phys.* **2002**, *91*, 9943–9947. [\[CrossRef\]](#)
63. Franco, V.; Conde, A.; Kuz'min, M.D.; Romero-Enrique, J.M. The magnetocaloric effect in materials with a second order phase transition: Are TC and Tpeak necessarily coincident? *J. Appl. Phys.* **2009**, *105*, 07A917. [\[CrossRef\]](#)
64. Koubaa, W.C.-R.; Koubaa, M.; Cheikhrouhou, A. Magnetic entropy change in the monovalent doping $\text{La}_{0.7}\text{Ba}_{0.2}\text{M}_{0.1}\text{MnO}_3$ ($M = \text{Na}, \text{Ag}, \text{K}$) manganites. *J. Mater. Sci.* **2009**, *44*, 1780–1786. [\[CrossRef\]](#)
65. Amano, M.E.; Betancourt, I.; Sánchez Llamazares, J.L.; Huerta, L.; Sánchez-Valdés, C.F. Mixed-valence $\text{La}_{0.80}(\text{Ag}_{1-x}\text{Sr}_x)_{0.20}\text{MnO}_3$ manganites with magnetocaloric effect. *J. Mater. Sci.* **2014**, *49*, 633–641. [\[CrossRef\]](#)
66. Ben Jemaa, F.; Mahmood, S.; Ellouze, M.; Hlil, E.K.; Halouani, F.; Bsoul, I.; Awawdeh, M. Structural, magnetic and magnetocaloric properties of $\text{La}_{0.67}\text{Ba}_{0.22}\text{Sr}_{0.11}\text{Mn}_{1-x}\text{FexO}_3$ nanopowders. *Solid State Sci.* **2014**, *37*, 121–130. [\[CrossRef\]](#)

67. Ben Rejeb, M.; Cheikhrouhou-Koubaa, W.; Koubaa, M.; Cheikhrouhou, A. Effect of elaborating method on magnetic and magnetocaloric properties of $\text{La}_{0.65}\text{Ca}_{0.35-x}\text{K}_x\text{MnO}_3$ ($0 \leq x \leq 0.2$) manganites. *J. Supercond. Nov. Magn.* **2015**, *28*, 839–846. [[CrossRef](#)]
68. Messaoui, I.; Riahi, K.; Kumaresavanji, M.; Cheikhrouhou Koubaa, W.; Cheikhrouhou, A. Potassium doping induced changes of magnetic and magnetocaloric properties of $\text{La}_{0.78}\text{Cd}_{0.22-x}\text{K}_x\text{MnO}_3$ ($x = 0.00, 0.10, 0.15$ and 0.20) manganites. *J. Magn. Magn. Mater.* **2018**, *446*, 108–117. [[CrossRef](#)]
69. Dhahri, A.; Dhahri, J.; Dhahri, E. Effect of potassium doping on physical properties of perovskites $\text{La}_{0.8}\text{Cd}_{0.2-x}\text{K}_x\text{MnO}_3$. *J. Alloys Compd.* **2010**, *489*, 9–12. [[CrossRef](#)]
70. Koubaa, W.C.-R.; Koubaa, M.; Cheikhrouhou, A. Effect of potassium doping on the structural, magnetic and magnetocaloric properties of $\text{La}_{0.7}\text{Sr}_{0.3-x}\text{K}_x\text{MnO}_3$ perovskite manganites. *J. Alloys Compd.* **2009**, *470*, 42–46. [[CrossRef](#)]
71. Franco, V.; Conde, A.; Romero-Enrique, J.M.; Blázquez, J.S. A universal curve for the magnetocaloric effect: An analysis based on scaling relations. *J. Phys. Condens. Matter* **2008**, *20*, 285207. [[CrossRef](#)]



© 2020 by the authors. Licensee MDPI, Basel, Switzerland. This article is an open access article distributed under the terms and conditions of the Creative Commons Attribution (CC BY) license (<http://creativecommons.org/licenses/by/4.0/>).